Journal of Power Sources 186 (2009) 508–514

Contents lists available at ScienceDirect

Journal of Power Sources

journal homepage: www.elsevier.com/locate/jpowsour

Nano $Li_4Ti_5O_{12}$–$LiMn_2O_4$ batteries with high power capability and improved cycle-life

Aurelien Du Pasquier[a,*], C.C. Huang[b], Timothy Spitler[c]

[a] Rutgers, The State University of New-Jersey, Energy Storage Research Group, Department of Materials Science and Engineering, 671, Highway 1, North Brunswick, NJ 08902, USA
[b] Hosokawa Micron Powder Systems, Hosokawa Micron International Inc., 10 Chatham Road, Summit, NJ 07901, USA
[c] Altair Nanotechnologies Inc., 204 Edison Way, Reno, NV 89502, USA

ARTICLE INFO

Article history:
Received 11 August 2008
Received in revised form 1 October 2008
Accepted 2 October 2008
Available online 17 October 2008

Keywords:
$LiMn_2O_4$
$Li_4Ti_5O_{12}$
Nanosized
Laminate
Li-ion battery
Carbon coating

ABSTRACT

We report the effects of electrode thickness, cathode particle size and morphology, cathode carbon coating matching ratio and laminate structure on the electrochemical characteristics of nanosized $Li_4Ti_5O_{12}$–$LiMn_2O_4$ batteries. We show that a correct adjustment of these parameters resulted in significant improvements in power capability and cycle-life of such devices, making them competitive, low-cost and safe battery chemistry for next generation Li-ion batteries. In addition, $Li_4Ti_5O_{12}$ reversible specific capacity beyond three Li-ions intercalation is reported.

1. Introduction

The lithium manganese spinel $LiMn_2O_4$ has been considered for over a decade the ideal replacement for $LiCoO_2$ currently used in mass produced Li-ion battery cathodes. The driving forces for this are (i) lower cost, about ten times lower than $LiCoO_2$, (ii) safer operation due to its steep end of charge signal, (iii) abuse tolerance due to its higher decomposition and oxygen release temperature than $LiCoO_2$ [1] and green attributes (easy disposal) due to its low toxicity. The above qualities make $LiMn_2O_4$ an ideal material for large scale production batteries that would power EV or HEV automobiles.

However, such promising attributes have been plagued by an insufficient cycle-life, retarding its implementation in commercial products. This low cycle-life originates from the interplay of at least two factors: in the bulk, Jahn-Teller distortion of the lattice causes electrochemical grinding [2], and on the surface, manganese dissolution [3] results in phase transformations, cathode and anode [4] passivation. In addition, these problems are exacerbated at elevated temperature, resulting in rapid battery failure.

As a consequence, $LiMn_2O_4$ has been a topic of intense research, and a large body of knowledge has been gained on this material. The consensus has been that both lattice stabilization by excess lithium and/or admetal doping [5], as well as surface modification [6,7] were necessary to obtain good cycle-life. [8]

The introduction of nanosized $Li_4Ti_5O_{12}$ (n-LTO) anodes for Li-ion batteries [9–11] has opened new avenues to the use $LiMn_2O_4$ spinel as next generation cathode material. It has been known for some time that better cycle-life could be obtained with $LiMn_2O_4$ when replacing the graphite anode with $Li_4Ti_5O_{12}$ in Li-ion batteries [12]. In 1998, Abraham reported $Li_4Ti_5O_{12}$/PAN electrolyte/$LiMn_2O_4$ passivation free batteries with excellent cycle-life and 60 Wh kg^{-1} energy density [13]. The reason for this good cycle-life is that, manganese plating from dissolved Mn^{2+} ions on a graphite anode causing its failure, is avoided. Further, redox shuttle mechanisms, with the graphitic anode passivation film decomposition products, enhances electrolyte acidification and manganese dissolution [14]. Because of its higher Li intercalation voltage (1.5 V versus Li^+, Li), $Li_4Ti_5O_{12}$ is not favoring this type of failure mechanisms [15]. In addition, the limited risk of Li-plating enables the design of batteries with large excess cathode capacity. This unique feature has been little investigated so far. However, it has important consequences, because it limits Li deintercalation in $LiMn_2O_4$. This enables to totally suppress the second phase

* Corresponding author. Tel.: +1 732 932 6850x602; fax: +1 732 932 6855.
E-mail address: adupasqu@rci.rutgers.edu (A. Du Pasquier).

0378-7753/$ – see front matter © 2008 Elsevier B.V. All rights reserved.
doi:10.1016/j.jpowsour.2008.10.018

formation causing Jahn-Teller distortion, without the need to modify the materials structure.

In this work, we have modified the particle size of $LiMn_2O_4$ to match its power rate capability with that of nanosized $Li_4Ti_5O_{12}$, and used carbon coating to improve its electrical connection. Then we optimized electrode formulation and investigated the impact of large excess cathode capacity on cycle-life and device energy density. In addition, this optimization has been performed on device-like prototypes in plastic Li-ion configuration and at elevated temperature. The benefit was to directly provide realistic measurements of life, power and energy density as close as possible to production devices.

2. Experimental

2.1. Active materials preparation

The anode used in this work was nanosized $Li_4Ti_5O_{12}$ produced by Altair patented process [16,17]. It measured 79 $m^2\ g^{-1}$ BET specific surface area, 5 μm average spherical aggregate diameter (Fig. 1a) and 20 nm average crystallite size (Fig. 1b).

A $LiMn_2O_4$ spinel commercially available (Aldrich) was modified for use with a high rate LTO anode. Elemental analysis showed slight Li excess, and a low level of Co doping (0.5 wt%, Mn basis). The particle size of the Aldrich material was first reduced to shards of ca. 50 nm. This resulted in a powder of 30 $m^2\ g^{-1}$ specific BET surface area. The crystal shards were then spray-dried at 100 °C in a Buchi bench-top unit, and annealed at various temperatures (400–900 °C). This resulted in grain growth and fusion of the crystals in spherical aggregates of 10 μm average diameter (Fig. 1c) and 2 $m^2\ g^{-1}$ specific BET area, but with a 500 nm primary crystallite size (Fig. 1d). Particle size distribution (PSD) analysis via Coulter LS230 confirmed the mean aggregate diameter of 10 μm. Their stability even after ultrasonication, indicated fusion of the primary crystals (Fig. 1e). Maximum crystallinity was obtained at 900 °C (Fig. 1f). The purpose of this processing was to reconcile the contradictory properties of fast Li^+ diffusion enabled by small crystallite size, with low manganese dissolution provided by a low BET specific

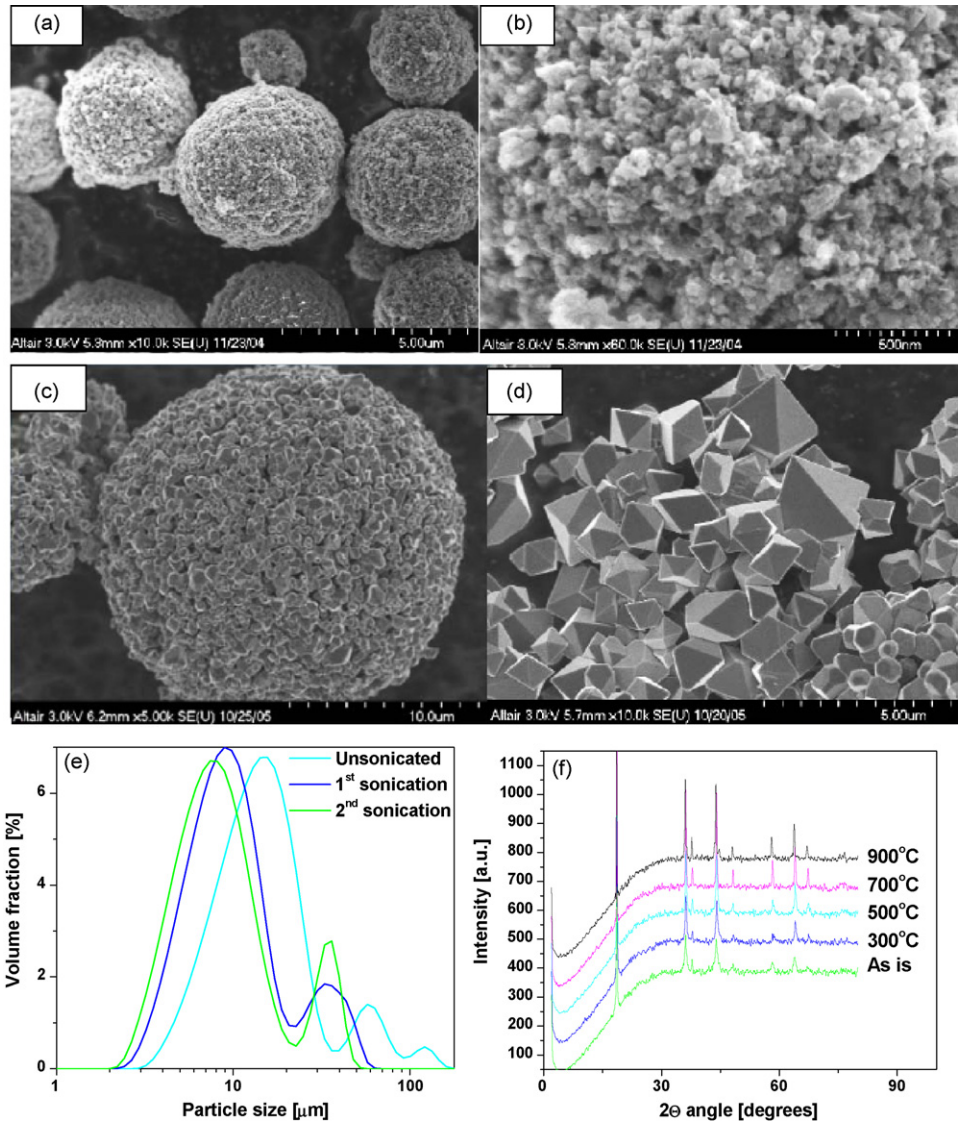

Fig. 1. Scanning electron microscopy (FESEM) micrographs of $Li_4Ti_5O_{12}$ spherical aggregate of 5 μm average diameter (a), surface of a $Li_4Ti_5O_{12}$ aggregate showing 20 nm fused $Li_4Ti_5O_{12}$ crystallites (b), $LiMn_2O_4$ spherical aggregate ~10 μm average size and 2 $m^2\ g^{-1}$ BET specific surface area (c), surface of the same aggregate after calcination at 900 °C showing > 500 nm average crystallite size and good self assembly (d), Particle size distribution (PSD) of 900 °C calcined aggregates before and after ultrasonication, proving fusion of the crystals together and 10 μm mean aggregate size (e), XRD information of $LiMn_2O_4$ aggregates at various calcination temperatures (f).

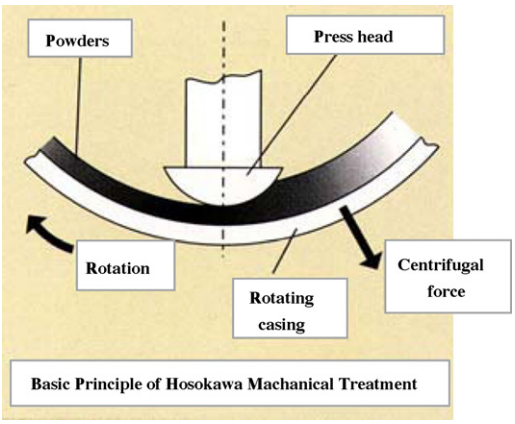

Fig. 2. Schematic of Hosokawa Mechano-Chemical Bonding Treatment.

Table 1
Summary of anode and cathode compositions.

Anode	Cathode
7 g of active material	6.5 g of active material
2 g Atofina 2801 PVDF-HFP	2.5 g Atofina 2801 PVDF-HFP
1 g SP carbon black	1 g E350 carbon black
5 g propylene carbonate	2.5 g propylene carbonate
30 g Acetone	30 g acetone

surface area. The final material (LMS1) had an unusually even grain size (primary particle) and consistent macrostructure not normally found in commercial materials. Its slow-rate specific capacity was 111 mAh g^{-1}.

Furthermore, applying Hosokawa Mechano-Chemical Bonding Technology, the nanosized $Li_4Ti_5O_{12}$ was carbon-coated with 2 wt% Super P carbon black (Timcal). The LMS1 material was carbon-coated with 1 wt% and 2 wt% Super P carbon black, respectively. These new carbon-coated LMS1 materials will be referred to as LMS1-1% and LMS1-2%.

The Hosokawa Mechano-Chemical Bonding Technology is a technique that can bond particles together using only mechanical energy in the dry phase. The basic operating principle of Mechano-Chemical Bonding Technology is as shown in Fig. 2. During the operation, the powders in the container are subjected to a centrifugal force and are securely pressed against the inner wall of rotating casing. The powders are further subjected to various mechanical forces, such as compression and shear forces, as they pass through a narrow gap between the casing wall and the press head. As a result, smaller guest particles are dispersed and bonded onto the surface of larger host particles without using binder of any kind. This is an environmentally friendly process to produce composite powders, especially nano-composites.

2.2. Plastic batteries fabrication

The electrodes were prepared by mixing the components reported in Table 1.

After mixing for 10 min in a laboratory blender, the slurry was doctor-blade cast on a Mylar substrate, and electrodes were cut on the Mylar in 2 in. × 3 in. size. After being weighed, the electrodes were bonded by hot lamination at 120 °C to aluminum grids etched and spray-coated with Acheson adhesive conductive coating. This ensured good bonding and low impedance of the electrode-collector interface. The cells were assembled by lamination at 120 °C to 25 (m Celgard microporous separator. They were of the bicell structure, which is: LTO/Al/LTO/sep/LMO/Al/LMO/sep/LTO/Al/LTO. They were dried overnight at 120 °C under vacuum in a glove box antechamber, then packaged and activated in a helium filled glove box. The activation electrolyte consisted of 1.5 mL acetonitrile, $LiBF_4$ 2 M with less than 20 ppm water contents.

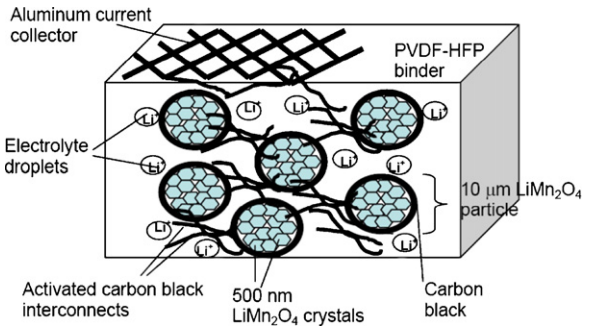

Fig. 3. Schematic of cathode structure.

2.3. Electrodes formulation and structure

From our experience, PVDF-HFP based electrodes require high binder and conductive carbon black (CB) contents for good cycle-life and rate capability of any active material. Those contents, however, should be minimized in order to maintain sufficient energy density. We also found that large BET area activated carbon black (ACB, 770 m^2 g^{-1}) provided better cycle-life and rate capability than same weight fraction of the CB material with 70 m^2 g^{-1} [18]. As a general rule, binding of materials with larger BET area requires more binder. Thus, we formulated a cathode recipe: 10 wt% ACB, 65 wt% $LiMn_2O_4$, 25 wt% PVDF-HFP. In this cathode, the carbon-coated $LiMn_2O_4$ particles are interconnected with the ACB fibrils to provide good electrical connection of the $LiMn_2O_4$ particles (Fig. 3).

By adopting this cathode formulation and reducing the anode thickness in half, a significant improvement in cycle-life and rate capability was achieved. This is simply a consequence of reducing diffusion impedance in the cathode, which is the life and rate limiting electrode in the system.

In doing this, some energy density had to be sacrificed. Table 2 is a recapitulation of electrode formulation and thickness impact on energy density, rate capability and cycle-life of the batteries.

2.4. Electrochemical testing protocol

After activation, the cell impedance was measured on a Solartron SI1260 impedance analyzer between 10,000 and 0.01 Hz signal of 20 mV amplitude. The cells were then transferred to a MACCOR4000 battery tester in a 25 °C environmental chamber for performance evaluation under the following testing protocol:

Table 2
Comparison of active material and cathode thickness effects in nano $Li_4Ti_5O_{12}/LiMn_2O_4$ batteries.

Cathode	Electrode loading (mA cm^{-2})	Energy density (Wh kg^{-1})	Matching ratio	Rate capability	Cycle-life
LMS1	1.1	52.5	1.47	Better	Better
LMS1 thin	0.57	41	1.81	Best	Best

- Discharge Ragone test: 1 C charges up to 3.2 V, 1, 5, 10, 20, 30, 40, 50, 60, 70, and 80 C discharges down to 1.0 V.
- Charge Ragone test: 1, 5, 10, 20, 30, 40, 50, 60, 70, and 80 C charges up to 3.2 V, 1 C discharges down to 1.0 V.
- Pause for impedance measurement.
- 1000 cycles with 20 C charges, 20 C discharges, 3.2–1 V voltage limits.
- Impedance measurement.

Since in most cases, the cathode is in excess capacity, the rate capability is expressed in mAh g^{-1} of the anode as function of C-rate, calculated from the theoretical capacity of the device, whichever the limiting electrode is. The energy density calculations are done on the basis of entire device weight (electrodes, collectors, separators, electrolyte) minus the packaging weight. The reason is that, since only one small battery laminate is packaged, the weight fraction of packaging material would be about 30% of the entire device weight.

3. Results and discussion

3.1. Matching ratio and carbon coating impact on cycle-life and capacity utilization

Using the ACB cathode formulation, we prepared three series of batteries using either LMS1, LMS1-1% or LMS1-2% cathodes, and the same anode thickness and formulation. In each series, we prepared 5 different matching ratios ranging from 0.75 to 2 times the theoretical matching ratio (TMR) by changing the cathode thickness. Table 3 is a recapitulation of the devices prepared and their characteristics.

The cycle-life of the materials was evaluated at 20 C charge–discharge rate over 1000 cycles for all the TMR prepared. The voltage limits were 1–3.2 V (5 s dwell) for all the samples. The curves of LTO capacity versus cycle number for LMS1, LMS1-1% and LMS1-2% cathode materials are respectively plotted on Fig. 4a–c. It is seen that the cycle-life increases when TMR increases, and also a slight improvement with carbon-coated cathodes. We can classify the cycle ability of these materials as follows: LMS1-2% > LMS1-1% > LMS1. However, at the highest matching ratios, we observe a rise in the capacity fade (Fig. 5). We attribute this effect to damage done to the anode by pushing its voltage too low, which can cause Li alloying with the aluminum current collector or Li over-intercalation in $Li_4Ti_5O_{12}$ phase.

Table 4
Highest device energy densities for all materials tested.

Cathode	TMR	Device energy @ 1 C (Wh kg^{-1})
LMS1	1.2	44.7
LMS1-1%	1.31	49.0
LMS1-2%	1.34	49.8

Fig. 6 indicates better anode utilization at higher matching ratio and at increased carbon contents. Surprisingly, the anode capacities measured are in some cases (high TMR, carbon coating) higher than the theoretical maximum of 174 mAh g^{-1} for LTO. This results in higher energy density for the carbon-coated devices. The energy density of the devices (package weight not included) is optimal when TMR ~1.3 enables best utilization of both electrodes (Fig. 7). Table 4 is listing the highest values measured at 1 C charge–discharge rate for all the materials tested.

Finally, we have plotted the Ragone plots (specific energy versus specific power) expressed in Wh kg^{-1} versus W kg^{-1} for all the cells tested (Fig. 8). At high discharge power, we measure 20 Wh kg^{-1} at 2000 W kg^{-1} average power on the entire discharge for the best devices. This is very promising since pulse discharge power, more relevant for EV and HEV applications, is generally greater than average discharge power. However, the carbon coating is slightly detrimental to the high rate discharge capacity, and the change in slope of the Ragone plot is indicative of a diffusion limitation caused by the carbon coating. At high charging rates (beyond 30 C), all the samples display a change in the slope of the rate capability plots. This suggests a diffusion limitation to the charge. However, our results indicate that a quasi full recharge can be performed at 20 C, i.e. 3 min (not shown here).

A better understanding of the improved cycle-life and over-theoretical capacity measured can be derived from the voltage profiles. We have plotted the discharge voltage curves (1–80 C) and their derivatives (1 C) for the devices LMS1#1&5, (resp. Figs. 9 and 10).

For all the samples, two major differences are noticed between the low matching ratio cells (#1) and the high matching ratio ones (#5). On the derivative curves, only one peak is visible for charge and discharge, while two peaks are visible at low matching ratio. This indicates that only the first phase of LMS is being utilized at high matching ratio. This implies a lower charging voltage and lower lithium deintercalation, which does result in better cathode cycle-life, and less outgassing. Secondly, we observe at high

Table 3
Characteristics of the cells built for the matching ratio and carbon coating study.

Sample ID	LTO[a] (mA cm^{-2})	LMS (mA cm^{-2})	Capacity (mAh)	TMR factor[b]	Cell weight[c] (g)
LMS1#1	0.579	0.859	33.5	0.75	4.74
LMS1#2	0.579	1.18	44.8	1.03	5.12
LMS1#3	0.579	1.38	44.8	1.2	5.08
LMS1#4	0.579	2.10	44.8	1.81	5.5
LMS1#5	0.602	2.49	44.8	2.06	5.67
LMS1-1%#1	0.602	0.966	37.5	0.80	4.72
LMS1-1%#2	0.602	1.23	46.6	1.02	4.89
LMS1-1%#3	0.602	1.57	46.6	1.31	5.13
LMS1-1%#4	0.602	1.93	46.6	1.61	5.51
LMS1-1%#5	0.602	2.37	46.6	1.97	5.84
LMS1-2%#1	0.602	0.877	33	0.70	4.76
LMS1-2%#2	0.602	1.29	46.6	1.04	4.94
LMS1-2%#3	0.602	1.66	46.6	1.34	5.29
LMS1-2%#4	0.602	0.113	46.6	1.63	5.58
LMS1-2%#5	0.602	0.137	46.6	1.98	5.77

Calculations are based on 160 mAh g^{-1} LTO, 111 mAh g^{-1} LMO.

[a] In the devices, the anode area is double the cathode area.

[b] TMR factor = theoretical matching ratio factor = (cathode capacity/anode capacity).

[c] Includes packaging weight.

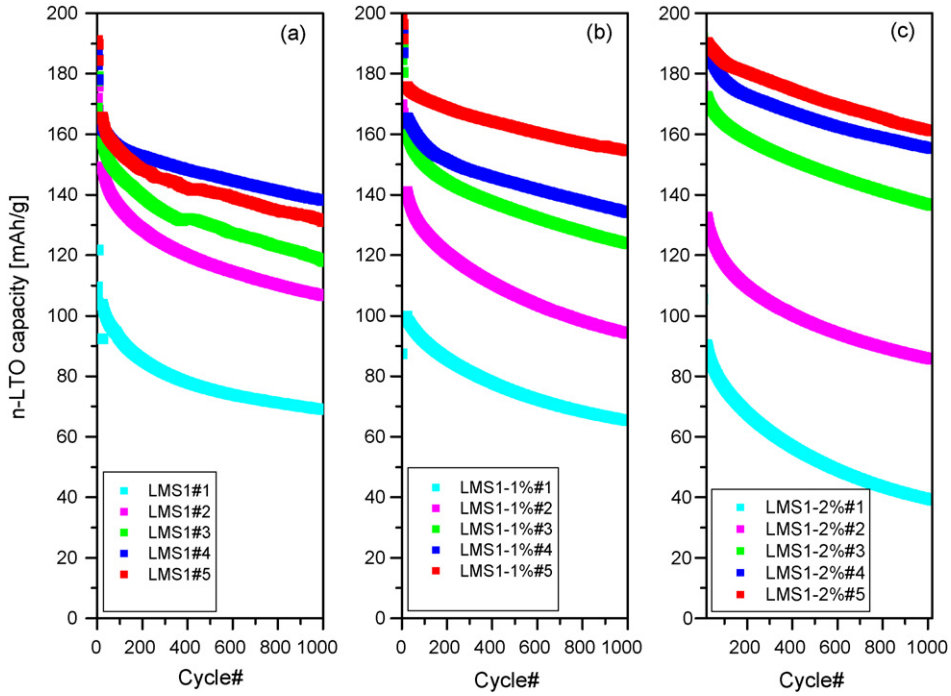

Fig. 4. n-LTO capacity fade versus cycle number for 20 C charge–discharge, 3.2–1 V room temperature (25 °C) cycling of all n-LTO/LMS1 (a), n-LTO/LMS1-1% (b) and n-LTO/LMS1-2% (c) cells at various matching ratios (cf. Table 2 for details).

matching ratio on the voltage profiles that there is a capacitive discharge from 3.2 to 2.6 V. This is analogous to the discharge of an electrochemical capacitor. We can partly attribute this effect to the double-layer capacitance of Li^+ ions adsorbed at the surface of the LTO anode. Indeed, the BET specific surface area of 79 $m^2\,g^{-1}$ for the LTO anode can account for a non negligible double-layer capacitance. Since there is extra capacity left in the cathodes for the high matching ratio cells, Li^+ ions start accumulating at the LTO surface once they have fully intercalated the LTO lattice. This effect could explain the over-theoretical capacity that we have observed on the rate capability plots. The double-layer capacitance of the anode can be calculated from the slope of the discharge plot between 3.2 and 2.6 V, according to the equation:

$$C = \frac{q}{V} = i \times \frac{dt}{dV} \quad (1)$$

Were q (C) is the charge stored in the double-layer and i (A) is the discharge current.

Then, knowing that:

$$\frac{1}{C_{tot}} = \frac{1}{C_{anode}} + \frac{1}{C_{cathode}} \quad (2)$$

We can consider that $C_{cathode}$ is infinite, as outlined by Conway in the treatment of asymmetric hybrid supercapacitors [19]. It results that $C_{tot} \sim C_{anode}$, and we can calculate a value of 12.6 F g^{-1} for the LTO anode. This is reasonable for its 79 $m^2\,g^{-1}$ BET specific surface area. However, this value does not fully explain the excess capacity up to 200 mAh g^{-1} LTO observed in some cases. While this surprising result mandates further investigation, we note that other authors have observed similar capacity for surface coated $Li_4Ti_5O_{12}$ overlithiated in the 0.6–0.01 V range [20]. The carbon appears to play a role in the higher capacity utilization, possibly through better

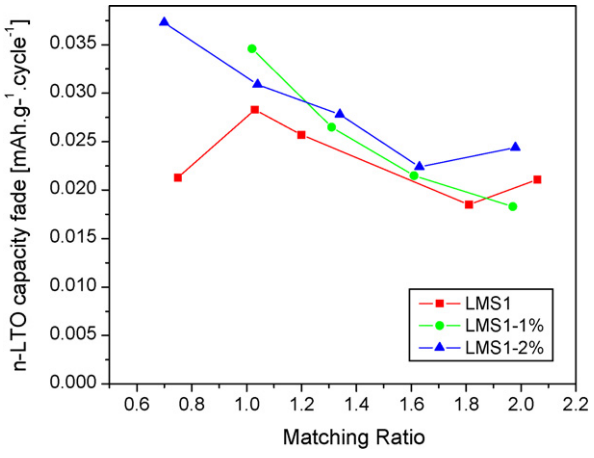

Fig. 5. Effect of matching ratio and carbon contents on the slope of capacity decay during 1000 cycles at 20 C charge–discharge for all the cells made.

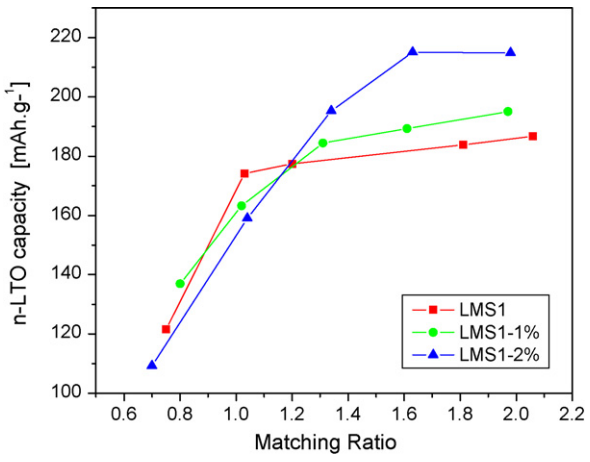

Fig. 6. n-LTO capacity at 10 C charge–discharge versus TMR for all the cells made.

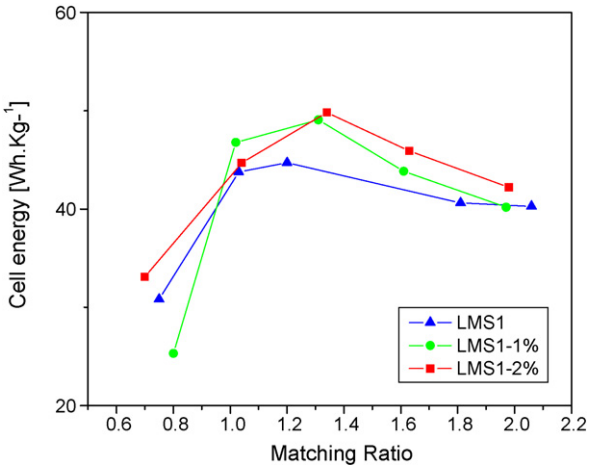

Fig. 7. Device gravimetric energy density at 10 C charge–discharge versus TMR for all the cells made.

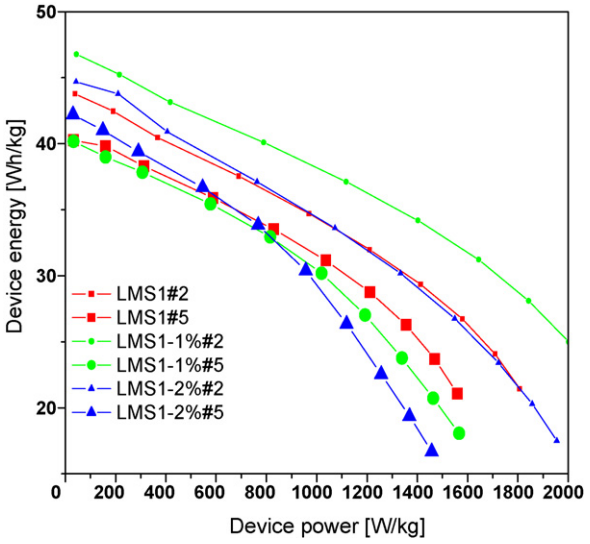

Fig. 8. Device Ragone plots for n-LTO/LMS1, LMS1-1% and LMS1-2% with TMR ~1 and TMR ~2.

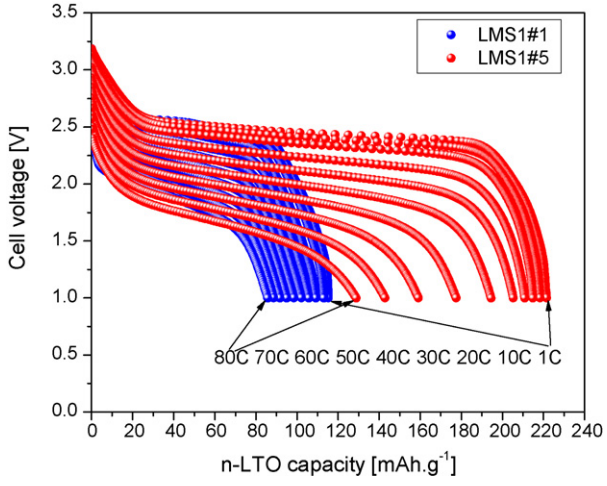

Fig. 9. Discharge voltage curves (1–80 C) for the devices LMS1#1&5.

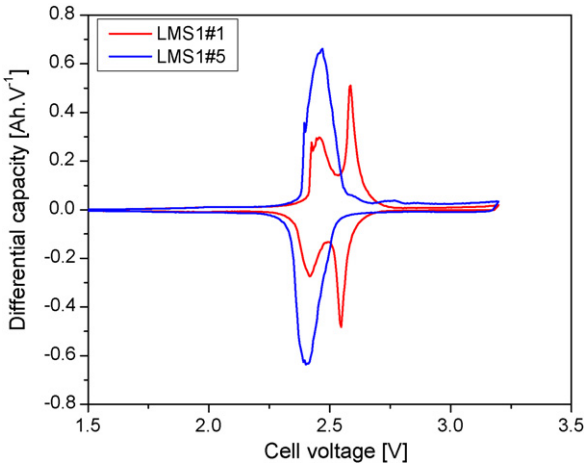

Fig. 10. Derivatives of the charge–discharge voltage profiles at 1 C for the devices LMS1&5.

electrolyte access and better electrical connection to the nanoparticles.

Li intercalation in the $Li_4Ti_5O_{12}$ spinel normally occurs in 8a sites and transfer to 16c sites [21]:

$$[Li]_{8a}[]_{16c}[Ti_{5/3}Li_{1/3}]_{16d}[O_4]_{32e} + Li^+ e^- \leftrightarrow []_{8a}[Li_2]_{16c}[Ti_{5/3}Li_{1/3}]_{16d}[O_4]_{32e} \quad (3)$$

When more than three lithium ions per formula are inserted, 8a, 8b and 48f sites could be occupied further since 16c sites are fully occupied already. The occupation of lithium at these sites would not change the spinel structure. A maximum reversible capacity of 242 mAh g^{-1} has already been reported for $Li_4Ti_5O_{12}$ [22]. In our case, the maximum capacity obtained was 215 mAh g^{-1}, which corresponds to ~$Li_{6.45}Ti_5O_{12}$.

3.2. Elevated temperature cycle-life and power capability

The major challenge with $LiMn_2O_4$-based Li-ion batteries has been their accelerated capacity fade at elevated temperature cycling and storage. In the present system, several innovations were suspected to have a positive impact on elevated temperature cycling: (i) absence of $LiPF_6$ in the electrolyte; (ii) carbon coating of the $LiMn_2O_4$; (iii) cathode excess capacity and (iv) anode less reductive than graphite. For these reasons, an elevated temperature investigation was undertaken.

Most of the batteries were made of inverted bicell laminates, that is anode/separator/cathode/separator/anode. For comparison, we built some batteries of the bicell structure, that is cathode/separator/anode/separator/cathode. In this case, the cathode area is doubled and the anode is halved. If the cathode is dominating the capacity fade, doubling its area should result in a lower capacity fade. The cells were cycled at 20 C rate, either at 25 or 55 °C. For comparison, we selected two of the best cycling inverted bicells (LMS1#5 and LMS1-1%#5) and subjected them to our standard cycling conditions (20 C, 3.2–1 V) but in a 55 °C chamber. This resulted in an acceleration of the capacity fade, as a well-known feature of the $LiMn_2O_4$ spinel. As expected, we observed an improved cycle-life at 55 °C for the bicells. More surprisingly, we also observed a very good cycle-life for the bicell with TMR = 1 at 25 °C, dispelling the notion that the Jahn-Teller effect was the major cause of capacity fade for the $LiMn_2O_4$ spinel. Indeed, our results indicate that the major cause of capacity fade is the impedance increase on the cathode caused by the formation of a resistive layer which is exacerbated when the time spent at elevated tempera-

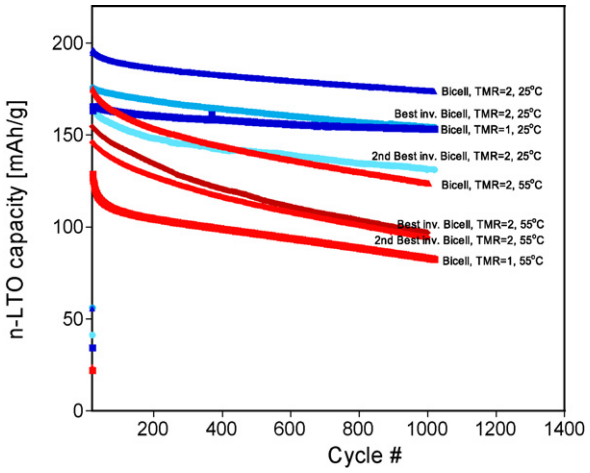

Fig. 11. Effect of matching ratio and battery laminate structure on capacity versus cycle number evolution during 20 C cycling at 25 or 55 °C.

ture and higher voltage increases. With this regard, the cells with TMR = 2 display less capacity fade at 55 °C because of their reduced charging voltage. Unfortunately, we also observed that the bicells had a reduced power capability (despite slightly thinner electrodes) compared with the inverted bicells. This is caused by the fact that the LTO anode, due to its lower electronic conductivity, is indeed rate limiting the system. Thus, when the anode area is doubled as in the inverted bicell, better rate capability is obtained.

The achievement of 1000 elevated temperature cycles with less than 50% capacity fade over that cycling period can be considered very encouraging with a LMS cathode (Fig. 11). In addition, we did not notice any significant outgassing of the cells that were cycled at 55 °C (usually visible as ballooning of the soft packaging).

4. Conclusions

The nano $Li_4Ti_5O_{12}/LiMn_2O_4$ battery has been developed in a direction that favors high power delivery and good cycle-life. The rate capability and number of charge–discharge cycles are, to the best of our knowledge, the highest ever measured for this type of battery. At 80 C, the best devices still utilized 160 mAh g^{-1} of the anode, versus 190 mAh g^{-1} at 1 C. In terms of device power and energy, this translates to 49 Wh kg^{-1} at 50 W kg^{-1}, and 20 Wh kg^{-1} at 2000 W kg^{-1}.

When extra capacity was present in the cathode, it did not cause lithium plating, but Li^+ adsorption at the $Li_4Ti_5O_{12}$ surface, resulting in over-theoretical capacity causing a supercapacitor-like discharge voltage profile from 3.2 to 2.6 V. This enabled to compensate for the loss in energy density caused by using thin electrodes. Large cathode excess (1.8 to 2× TMR) and carbon coating were also advantageous by increasing cycle-life and anode utilization, with little penalty in energy density. The cycle-life achieved was satisfactory, with 18.3 mAh g^{-1} n-LTO capacity fade over 1000 cycles for TMR ~2 in the 1% carbon-coated LMS1 sample. Elevated temperature cycling (55 °C) did not result in a dramatic capacity failure, but an increase in the fade slope, with steady and predictable behavior. Lower capacity fade but also lower power capability was obtained with the bicell structure, that is a doubled cathode area with respect to the anode area. In this case, excellent cycle-life was also obtained at room temperature in cells with a 1 to 1 capacity matching ratio. This important result indicates that low dopant $LiMn_2O_4$ spinel can be fully utilized over extended numbers of fast cycles when the cathode passivation layer is not given enough time to grow. These attributes, combined with an extremely fast charge capability (full charge possible in 3 min) already make the device competitive for applications such as power tools and digital cameras. For more demanding applications such as EV and HEV, a wider temperature range is possible by the adoption of multi-component carbonate-based electrolytes, binders less prone to swelling, and high Co, Al or F doped manganese spinels with lowered Mn dissolution.

Acknowledgements

The authors would like to thank the National Science Foundation for the financing of this study under the SBIR phase II contract DMI-0522287. One of the authors (ADP) would like to thank John Gural and Irene Plitz for coating the aluminum current collectors used in this work.

Thank you to Nathalie Pereira for proofreading the manuscript.

References

[1] I. Belharouak, Y.K. Sun, W. Lu, et al., J. Electrochem. Soc. 154 (2007) A1083–A1087.
[2] K.Y. Chung, K. Kim, Electrochim. Acta 49 (2004) 3327–3337.
[3] A. Du Pasquier, A. Blyr, P. Courjal, D. Larcher, G. Amatucci, B. Gérand, J.M. Tarascon, J. Electrochem. Soc. 146 (1999) 428–436.
[4] N. Kumagai, S. Komaba, Y. Kataoka, M. Koyanagi, Chem. Lett. 29 (2000) 1154–1155.
[5] G.G. Amatucci, N. Pereira, T. Zheng, J.-M. Tarascon, J. Electrochem. Soc. 148 (2001) A171–A182.
[6] Y. Sun, Z. Wang, L. Chen, X. Huang, J. Electrochem. Soc. 150 (2003) A1294–A1298.
[7] J.S. Gnanaraj, V.G. Pol, A. Gedanken, D. Aurbach, Electrochem. Commun. 5 (2003) 940–945.
[8] G. Amatucci, J.-M. Tarascon, J. Electrochem. Soc. 149 (2002) K31–K46.
[9] L. Kavan, J. Procházka, T. Spitler, M. Kalbáč, M. Zukalová, T. Drezen, M. Grätzel, J. Electrochem. Soc. 150 (2003) A1000–A1007.
[10] G.G. Amatucci, F. Badway, A. Du Pasquier, T. Zheng, J. Electrochem. Soc. 148 (2001) A930–A939.
[11] G.X. Wang, D.H. Bradhurst, S.X. Dou, H.K. Liu, J. Power Sources 83 (1999) 156–161.
[12] G. Amatucci, A. Du Pasquier, A. Blyr, T. Zheng, J.-M. Tarascon, Electrochim. Acta 45 (1999) 255–271.
[13] D. Peramunage, K.M. Abraham, J. Electrochem. Soc. 145 (1998) 2615–2622.
[14] J. Kim, K. Amine, Meeting Abstr. (2004) 289.
[15] D.P. Abraham, E.M. Reynolds, E. Sammann, A.N. Jansen, D.W. Dees, Electrochim. Acta 51 (2005) 502–510.
[16] T. Spitler, et al., United States Patent 6,881,393 (2005).
[17] T. Spitler, et al., United States Patent 6,890,510 (2005).
[18] A. Du Pasquier, I. Plitz, J. Gural, F. Badway, G.G. Amatucci, J. Power Sources 136 (2004) 160–170.
[19] W.G. Pell, B.E. Conway, J. Power Sources 136 (2004) 334–345.
[20] H. Ge, N. Li, D. Li, C. Dai, D. Wang, Electrochem. Commun. 10 (2008) 719–722.
[21] T. Ohzuku, A. Ueda, N. Yamamoto, J. Electrochem. Soc. 142 (1995) 1431.
[22] M. Venkateswarlu, C.H. Chen, J.S. Do, C.W. Lin, T.C. Chou, B.J. Hwang, J. Power Sources 146 (2005) 204.